LETTER

doi:10.1038/nature14295

Square ice in graphene nanocapillaries

G. Algara-Siller[1], O. Lehtinen[1], F. C. Wang[2], R. R. Nair[3], U. Kaiser[1], H. A. Wu[2], A. K. Geim[3] & I. V. Grigorieva[3]

Bulk water exists in many forms, including liquid, vapour and numerous crystalline and amorphous phases of ice, with hexagonal ice being responsible for the fascinating variety of snowflakes[1,2]. Much less noticeable but equally ubiquitous is water adsorbed at interfaces and confined in microscopic pores. Such low-dimensional water determines aspects of various phenomena in materials science, geology, biology, tribology and nanotechnology[3–8]. Theory suggests many possible phases for adsorbed and confined water[9–17], but it has proved challenging to assess its crystal structure experimentally[17–23]. Here we report high-resolution electron microscopy imaging of water locked between two graphene sheets, an archetypal example of hydrophobic confinement. The observations show that the nanoconfined water at room temperature forms 'square ice'—a phase having symmetry qualitatively different from the conventional tetrahedral geometry of hydrogen bonding between water molecules. Square ice has a high packing density with a lattice constant of 2.83 Å and can assemble in bilayer and trilayer crystallites. Molecular dynamics simulations indicate that square ice should be present inside hydrophobic nanochannels independently of their exact atomic nature.

Many molecular dynamics (MD) studies[9–17] have explored the structure of low-dimensional water and predicted a great variety of phases, with results sensitive to modelled conditions and sometimes appearing conflicting. For example, buckled monolayer ice[10] and flat hexagonal ice[14,16,23], respectively, were found inside hydrophilic and hydrophobic nanochannels below room temperature, whereas no in-plane order was observed for water inside simulated mica (hydrophilic) and graphite (hydrophobic) nanochannels at and above room temperature[13,15]. A close analogue of planar square ice was seen in MD simulations of water inside carbon nanotubes[9,11,12,18], where water molecules form a monolayer that can be viewed as a sheet of square ice rolled up into a quasi-one-dimensional cylinder. Neutron studies[18] revealed features consistent with the existence of such 'ice nanotubes', which melted above 50 K. Two-dimensional (2D) ices have also been found experimentally on the surfaces of mica and graphite[19–23]. The studies using scanning probe microscopy[20–22] and electron crystallography[19,23] show that near-surface water can form correlated, solid-like layers. As for their intralayer structure, information is only available for 2D ices grown below 150 K, which were found to be hexagonal, with in-plane coordination similar to that of bulk ices[19,23].

For this study, we deposited a graphene monolayer on a standard transmission electron microscopy (TEM) grid, exposed it to a small amount of water and covered it with another graphene monolayer[24,25] (see 'Sample preparation' in Methods for full details). Most of the water was squeezed out by van der Waals forces that brought the two graphene layers together, but some water remained trapped in numerous pockets of submicrometre size (Extended Data Fig. 1). We also prepared reference samples similar to those described in ref. 24, in which a larger amount of deposited water resulted in three-dimensional droplets of ~10–100 nm in thickness (Extended Data Fig. 2). The TEM studies were carried out using transmission electron microscope FEI TITAN 80-300 operated at 80 kV.

Typical atomic-resolution images of graphene-confined water are shown in Fig. 1a and Extended Data Figs 1b and 3a–i. High-contrast dark spots correspond to oxygen and indicate the positions of the water molecules. Hydrogen atoms yield too little contrast to be resolved even by the state-of-the-art TEM. The encapsulating graphene layers are seen in some parts of the images as a faint background with hexagonal symmetry[25,26]. The images can easily be improved by digitally subtracting the contribution from the encapsulating graphene[25], but we avoid this additional processing in view of the quality and contrast of our raw data, which clearly show water forming a regular square lattice. Fast Fourier transform analysis of the ice lattice yielded a distance a between nearest-neighbour oxygen atoms of 2.83 ± 0.03 Å (Fig. 1a), with no alignment with the graphene lattice observed. We note that the atomic-resolution imaging of interfacial ice is possible only because of the use of graphene: its low atomic number and crystallinity result in a minimal background and high contrast for oxygen atoms[24,26], and its mechanical strength, high thermal and high electrical conductivity and chemical stability protect encapsulated water from sublimation and the adverse effects of electron irradiation[25,27] (see 'Transmission electron microscopy' in Methods).

To confirm that the observed square lattice is indeed formed by water, we acquired electron energy loss spectra (EELS) from areas with ice such as shown in Fig. 1a and from areas without any visible amount of trapped water. Figure 1b compares typical spectra around the oxygen K-edge (which are sensitive to the state of water[28]). The ice-free areas show little oxygen signal. In contrast, square ice exhibits a spectrum with an overall shape that is qualitatively similar to EELS for three-dimensional ices such as hexagonal I_h and diamond cubic I_c ices[28] (inset of Fig. 1b). But there are also notable differences, such as the approximately 6-eV difference between the main EELS peak positions for square ice and for three-dimensional ices. The energy separation between the main and secondary EELS peaks gives an independent estimate of the oxygen–oxygen distance of about 2.8 Å (see 'EELS analysis' in Methods), in agreement with the observed lattice constant. Also, EELS measured for large water droplets found in our reference samples agree with the spectra expected for mixtures of liquid water and water vapour (Extended Data Fig. 2b).

The square ice is found to be highly mobile under the electron beam (Extended Data Fig. 3 and Supplementary Video), with uniform monolayers starting to break into crystallites about 10 nm across with sharp crystallographic edges after the first few seconds of imaging. The crystallites change shape, split and merge, with the frequency of reconstruction increasing with beam current. Grain boundaries and dislocations form as the crystallites move and coalesce, but high crystallinity is preserved with no sign of ice melting or amorphization (Extended Data Fig. 3). The strong TEM contrast variations seen in such images arise from differences in ice layer numbers, as illustrated in Fig. 2, where equal-height steps in contrast correspond to changes from monolayer to bilayer and to trilayer ice (see Extended Data Fig. 4 for details). Using the quantified contrast to examine many images and videos of 2D ice, we found that three is the maximum number of ice layers observed in our experiments.

The TEM images show unambiguously that water molecules in the few-layer ice are AA stacked, with oxygen atoms in adjacent layers sitting directly on top of each other. The AA stacking is evident when

[1]Central Facility for Electron Microscopy, Group of Electron Microscopy of Materials Science, University of Ulm, 89081 Ulm, Germany. [2]Chinese Academy of Sciences Key Laboratory of Mechanical Behavior and Design of Materials, Department of Modern Mechanics, University of Science and Technology of China, Hefei, Anhui 230027, China. [3]School of Physics and Astronomy, University of Manchester, Manchester M13 9PL, UK.

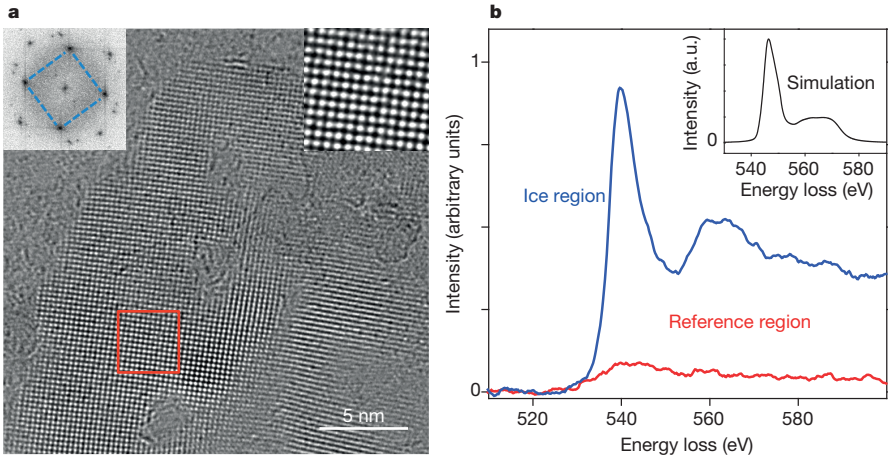

Figure 1 | Square ice. a, Part of a large water pocket (see Extended Data Fig. 1a). Several such pockets were studied. Irregular structures are hydrocarbon contamination. The top right inset shows a magnified image of the area outlined in red. The top left inset shows a Fourier transform of the entire image, with four first-order maxima of the square lattice; the square symmetry is highlighted by the blue lines; the two hexagonal sets come from encapsulating graphene. **b**, EELS from areas containing 2D ice and no visible water. Both spectra come from similar size areas (~100 nm). The inset shows the simulated EELS for three-dimensional ices (I_c and I_h exhibit similar spectra)[28].

comparing experimental (Fig. 2a) with simulated (Fig. 2b, c) TEM images: AB stacking results in oxygen atoms in the second layer occupying the sites between oxygen sites in the first and third layers, which in turn results in a perceived 45° rotation of the water lattice and reduction in the projected oxygen spacing. Furthermore, the reduced spacing leads to lower contrast and, consequently, a qualitatively different appearance of AB bilayers (Fig. 2c) compared to the experimental images (Fig. 2a). Note that stacking controls the difference between different phases of bulk ice. For example, hexagonal and diamond cubic ices both consist of puckered hexagonal layers but have AB and ABC stacking, respectively. In all bulk ice phases the bonding between water molecules follows so-called 'ice rules' that require a tetrahedral coordination of hydrogen bonds[1,2]. In contrast, the few-layer ice we report here corresponds to 90° hydrogen bonding both within and between layers.

To support our TEM observations, we carried out MD simulations of water in graphene nanocapillaries (Methods). Distances between the carbon plane centres were varied from 6.5 Å to 11.5 Å, to accommodate one to three monolayers of water (Extended Data Fig. 5). For narrow 2D channels that can accommodate only one monolayer, we always found square ice with $a = 2.81 \pm 0.02$ Å, in agreement with experiment (Fig. 2d and Extended Data Fig. 6). This MD result is robust, showing little dependence on the capillary width, applied pressure or whether graphene sheets were made rigid, flexible or freely moving (Methods).

For wider capillaries that accommodate two or three monolayers of water, no in-plane ordering could be found under simulated ambient conditions. Instead, water molecules form a distinct layered structure but locally maintain the tetrahedral arrangement of hydrogen bonds both within and between the layers (Extended Data Fig. 7a, b). We believe

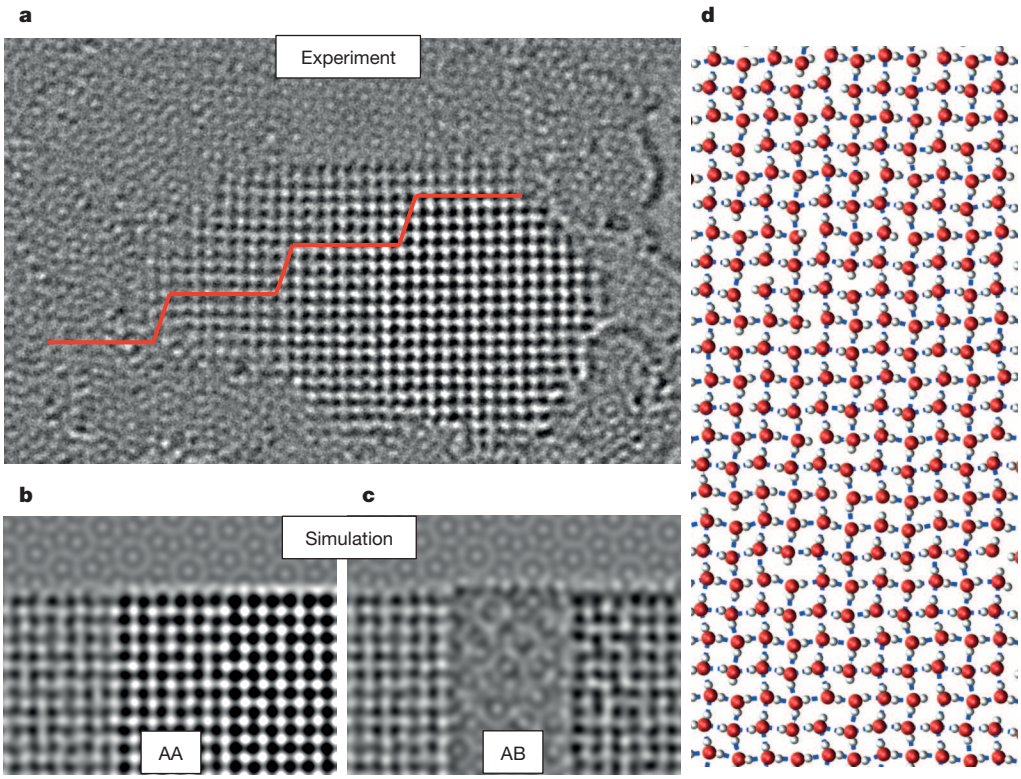

Figure 2 | Few-layer ice and its stacking order. a, Isolated crystallite with a varying number of layers. The moiré pattern (seen clearly at the top) is due to encapsulating graphene. The red curve shows changes in the contrast averaged over the corresponding parts of the image (Methods). The changes occur in quantized steps. **b** and **c**, Simulated TEM images for monolayer, bilayer and trilayer ice with AA and AB stacking, respectively. The AA stacking agrees well with our experimental images whereas the AB stacked ice results in the qualitatively different appearance. **d**, Typical snapshot of MD-simulated water in a graphene nanocapillary. Red and white circles show oxygen and hydrogen atoms, respectively; short blue lines indicate hydrogen bonds within H_2O.

this apparent disagreement between simulation and experiment arises because adhesion between the encapsulating graphene sheets imposes pressure on the water as it is squeezed into a small volume, and this needs to be taken into account in simulations. As illustrated in Extended Data Fig. 8, this pressure—we refer to it as van der Waals pressure—can be estimated from the energy gain due to such squeezing according to $P_W \approx E_W/d \approx 1$ GPa, where $E_W \approx 20$–30 meV Å^{-2} is the adhesion energy[29,30] and $d \approx 3.5$ Å is a typical interlayer distance. This estimate agrees with our simulations of hydrostatic pressure acting on a gas trapped between freely moving graphene sheets (Methods). To mimic the effect of van der Waals pressure, we ran simulations with an applied external pressure P (as illustrated in Extended Data Fig. 5) and found a pronounced transition from in-plane disorder at low P to layered ice at $P > 1$ GPa (Extended Data Figs 7 and 9). The layered ice exhibited the same lattice constant ($a = 2.81 \pm 0.02$ Å) as the monolayer, in agreement with experiment.

The MD simulations fail, however, in reproducing the observed AA stacking and instead show a tendency for crystals with AB stacking or no interlayer order (Extended Data Figs 7 and 9). The disagreement is perhaps not surprising when we consider that as P increases to reach the crystallization transition, hydrogen bonds switch to the in-plane configuration (Extended Data Figs 7d and 9b) so that coupling between monolayers of square ice becomes van-der-Waals-like. Such weak coupling is known to be extremely difficult to accurately account for theoretically. Moreover, in the experiment the graphene-confined ice exhibits sharp steps between terraces (see Fig. 2), which can result in extra lateral forces acting on different layers not considered in the simulations. Finally, our simulations for bilayer and trilayer ice yield an interlayer separation of $c = 2.8 \pm 0.3$ Å, which gives a crystal lattice close to the simple cubic structure ($c = a$) and a density approximately 1.5 times higher than that of common ice. But the exact structure is still, strictly speaking, tetragonal because of the qualitative difference between interlayer and intralayer bonding (Extended Data Figs 7 and 9).

The 2D ice we report here exhibits coordination that is qualitatively different from the conventional tetrahedral coordination in bulk and surface ices. We expect it to be common inside hydrophobic nanocapillaries under ambient conditions, basically because the water–surface interaction in such confinement is much weaker than the interaction between water molecules. Indeed, our MD simulations yield the same square lattices inside non-graphene capillaries with widely varying hydrophobicity (Extended Data Fig. 10). The existence of low-dimensional ice at room temperature has been proposed to explain the fast water permeation through hydrophobic nanocapillaries, including carbon nanotubes and graphene-based membranes, and our report supports this idea. The van der Waals pressure invoked here may be important in many nanoscale phenomena.

Online Content Methods, along with any additional Extended Data display items and Source Data, are available in the online version of the paper; references unique to these sections appear only in the online paper.

Received 10 October 2014; accepted 4 February 2015.

1. Petrenko, V. F. & Whitworth, R. W. *Physics of Ice* (Oxford Univ. Press, 2002).
2. Malenkov, G. Liquid water and ices: understanding the structure and physical properties. *J. Phys. Condens. Matter* **21,** 283101 (2009).
3. Israelachvili, J. & Wennerström, H. Role of hydration and water structure in biological and colloidal interactions. *Nature* **379,** 219–225 (1996).
4. Brown, G. E. How minerals react with water. *Science* **294,** 67–69 (2001).
5. Appelo, C. A. J. & Postma, D. *Geochemistry, Groundwater and Pollution* (Taylor & Francis, 2005).
6. Chandler, D. Interfaces and the driving force of hydrophobic assembly. *Nature* **437,** 640–647 (2005).
7. Verdaguer, A., Sacha, G. M., Bluhm, H. & Salmeron, M. Molecular structure of water at interfaces: wetting at the nanometer scale. *Chem. Rev.* **106,** 1478–1510 (2006).
8. Chaplin, M. F. in *Adsorption and Phase Behaviour in Nanochannels and Nanotubes* (eds Dunne L. & Manos, G.) 241–255 (Springer, 2010).
9. Kalra, A., Garde, S. & Hummer, G. Osmotic water transport through carbon nanotube membranes. *Proc. Natl Acad. Sci. USA* **100,** 10175–10180 (2003).
10. Zangi, R. & Mark, A. E. Monolayer ice. *Phys. Rev. Lett.* **91,** 025502 (2003).
11. Maniwa, Y. *et al.* Ordered water inside carbon nanotubes: formation of pentagonal to octagonal ice-nanotubes. *Chem. Phys. Lett.* **401,** 534–538 (2005).
12. Takaiwa, D., Hatano, I., Koga, K. & Tanaka, H. Phase diagram of water in carbon nanotubes. *Proc. Natl Acad. Sci. USA* **105,** 39–43 (2008).
13. Giovambattista, N., Rossky, P. J. & Debenedetti, P. G. Phase transitions induced by nanoconfinement in liquid water. *Phys. Rev. Lett.* **102,** 050603 (2009).
14. Han, S., Choi, M. Y., Kumar, P. & Stanley, H. E. Phase transitions in confined water nanofilms. *Nature Phys.* **6,** 685–689 (2010).
15. Srivastava, R., Docherty, H., Singh, J. K. & Cummings, P. T. Phase transitions of water in graphite and mica pores. *J. Phys. Chem. C* **115,** 12448–12457 (2011).
16. Bai, J. & Cheng Zeng, X. Polymorphism and polyamorphism in bilayer water confined to slit nanopore under high pressure. *Proc. Natl Acad. Sci. USA* **109,** 21240–21245 (2012).
17. Nair, R. R., Wu, H. A., Jayaram, P. N., Grigorieva, I. V. & Geim, A. K. Unimpeded permeation of water through helium-leak–tight graphene-based membranes. *Science* **335,** 442–444 (2012).
18. Kolesnikov, A. I. *et al.* Anomalously soft dynamics of water in a nanotube: a revelation of nanoscale confinement. *Phys. Rev. Lett.* **93,** 035503 (2004).
19. Yang, D. S. & Zewail, A. H. Ordered water structure at hydrophobic graphite interfaces observed by 4D, ultrafast electron crystallography. *Proc. Natl Acad. Sci. USA* **106,** 4122–4126 (2009).
20. Xu, K., Cao, P. & Heath, J. R. Graphene visualizes the first water adlayers on mica at ambient conditions. *Science* **329,** 1188–1191 (2010).
21. He, K. T., Wood, J. D., Doidge, G. P., Pop, E. & Lyding, J. W. Scanning tunnelling microscopy study and nanomanipulation of graphene-coated water on mica. *Nano Lett.* **12,** 2665–2672 (2012).
22. Zheng, Y., Su, C., Lu, J. & Loh, K. P. Room-temperature ice growth on graphite seeded by nano-graphene oxide. *Angew. Chem. Int. Ed.* **52,** 8708–8712 (2013).
23. Kimmel, G. A. *et al.* No confinement needed: observation of a metastable hydrophobic wetting two-layer ice on graphene. *J. Am. Chem. Soc.* **131,** 12838–12844 (2009).
24. Yuk, J. M. *et al.* High-resolution EM of colloidal nanocrystal growth using graphene liquid cells. *Science* **336,** 61–64 (2012).
25. Algara-Siller, G., Kurasch, S., Sedighi, M., Lehtinen, O. & Kaiser, U. The pristine atomic structure of MoS_2 monolayer protected from electron radiation damage by graphene. *Appl. Phys. Lett.* **103,** 203107 (2013).
26. Meyer, J. C., Girit, C. O., Crommie, M. F. & Zettl, A. Imaging and dynamics of light atoms and molecules on graphene. *Nature* **454,** 319–322 (2008).
27. Dubochet, J., Lepault, J., Freeman, R., Berriman, J. A. & Homo, J.-C. Electron microscopy of frozen water and aqueous solutions. *J. Microsc.* **128,** 219–237 (1982).
28. Kobayashi, K., Koshino, M. & Suenaga, K. Atomically resolved images of I_h ice single crystals in the solid phase. *Phys. Rev. Lett.* **106,** 206101 (2011).
29. Björkman, T., Gulans, A., Krasheninnikov, A. V. & Nieminen, R. M. Van der Waals bonding in layered compounds from advanced density-functional first-principles calculations. *Phys. Rev. Lett.* **108,** 235502 (2012).
30. Koenig, S. P., Boddeti, N. G., Dunn, M. L. & Bunch, J. S. Ultrastrong adhesion of graphene membranes. *Nature Nanotechnol.* **6,** 543–546 (2011).

Supplementary Information is available in the online version of the paper.

Acknowledgements This work was supported by the DFG (Germany), the European Research Council, the EU Graphene Flagship, the National Natural Science Foundation of China, the Ministry of Science, Research and Arts of Baden-Wuerttemberg (Germany), the Office of Naval Research, the Air Force Office of Scientific Research, the Anhui Provincial Natural Science Foundation (China), the Finnish Cultural Foundation and the Fundamental Research Funds for the Central Universities of China. MD simulations were carried out at Supercomputing Center of the University of Science and Technology of China.

Author Contributions U.K., I.V.G and A.K.G. proposed and directed the project. G.A.-S. and O.L. designed the experiments and samples, performed TEM measurements and analysed them. H.A.W. and F.C.W. carried out MD simulations (with feedback from A.K.G.). I.V.G. and A.K.G. wrote the manuscript with help from all the authors.

Author Information Reprints and permissions information is available at www.nature.com/reprints. The authors declare no competing financial interests. Readers are welcome to comment on the online version of the paper. Correspondence and requests for materials should be addressed to I.V.G. (irina.grigorieva@manchester.ac.uk), U.K. (ute.kaiser@uni-ulm.de) or H.A.W. (wuha@ustc.edu.cn).

METHODS

Sample preparation. Graphene monolayers were grown on Cu foils by chemical vapour deposition and then transferred onto gold Quantifoil grids (Au mesh covered with an amorphous carbon film having a dense array of holes with a diameter of 1.2 μm). Importantly, a thin layer of Pt was deposited on the TEM grids before graphene transfer in order to reduce hydrocarbon contamination[31]. For the transfer, several Quantifoil grids were immersed in isopropanol and then placed 'face down' onto a piece of graphene on copper about 1 cm^2 in size. As the isopropanol evaporated, the amorphous carbon film of the TEM grid came into contact with graphene and became attached to it[32]. After that the assembly was floated on the surface of ammonium peroxodisulfate for several hours until all copper was slowly etched away, leaving free-floating graphene with several TEM grids attached to it. This was broken into pieces, with one grid attached to each, washed in water and isopropanol and left to dry in air at room temperature. After that 1 μl of deionized water was carefully cast on top of one of the grids, and another graphene-covered grid was placed on top, covering the water droplet. The resulting sandwich was left to dry under ambient conditions overnight, during which time the water drop slowly evaporated, bringing the two graphene layers together and gradually squeezing the liquid out so that only a small amount of adsorbed water remained captured in between the graphene sheets.

TEM. The use of both a relatively low operating voltage (80 keV) and the aberration correction were essential in our study: higher voltages are known to produce knock-on damage in graphene[33] and the aberration correction, even at relatively low acceleration voltages, allows atomic-resolution imaging of both graphene and water. The spherical aberration coefficient was set to 30 μm and the sample was imaged at Scherzer focus, resulting in dark atom contrast. The background pressure in the microscope was $<10^{-8}$ mbar, and all experiments were carried out at room temperature. Aberration-corrected high-resolution TEM images were acquired at a dose of 3×10^4 electrons per nm^2 and an exposure time of ~1 s per frame. The exposure of the studied area before acquisition of the reported images was approximately 600 electrons per nm^2. No notable heating by the electron beam is expected under these operating conditions. Indeed, for amorphous carbon films under similar experimental conditions, the heating was estimated to be ~1 K (ref. 34). As thermal conductivity of graphene is 3,000 times higher than that of amorphous carbon, we expect even less heating in our case. This agrees with our observation that the appearance of square ice did not qualitatively change with increasing or decreasing of the beam current.

The majority of our samples remained intact during the relatively long exposures to the electron beam (typically, 10–20 min); in a few cases only, we noticed etching of graphene[27,33–36]. This is in contrast to the earlier work on frozen aqueous samples that suffered from fast sublimation under the electron beam[27,28,37]. The high stability of 2D ice is due to graphene encapsulation. The highly conductive graphene layers (both electrically and thermally) provide an efficient channel for absorbing and rapidly dissipating the energy introduced by electron impacts, thus reducing the damage to ice crystals. This effect of graphene encapsulation was recently demonstrated in TEM studies[25,38] of monolayer MoS_2, a radiation-sensitive material. The encapsulation reduced the damage rate by nearly three orders of magnitude as compared to non-encapsulated MoS_2. Similarly, graphene capillaries in the present work served not only as a confinement channel but also as protection against the beam damage, which enabled us to observe the ice crystals without immediately evaporating or destroying them.

EELS analysis. Electron energy loss spectra[39,40] were acquired using GIF Quantum ER filter in the diffraction mode (convergence angle of 1.8 mrad and collection angle of 4.4 mrad). The spectra were recorded with exposure and integration times of 5 s and 200 s, respectively. A low pass filter (two pixels) and linear background subtraction were applied. All EELS showed prominent signals from carbon and oxygen. Hydrogen is not detectable with the instrument. No other elements could be detected, except for a small amount of Si that is commonly present in all areas because of contamination during sample preparation[41].

The overall appearance of EELS curves allows us to distinguish immediately between ice and mixtures of liquid water and water vapour (compare Figure 1b and Extended Data Fig. 2). Furthermore, bulk ices such as I_c and I_h have rather similar spectra[28], more similar to each other than to the observed EELS for square ice. This is understandable given that both I_c and I_h consist of puckered hexagonal layers, which is different from the planar square configuration. We have also used the spectral positions of the main and secondary peaks (see Fig. 1b) to estimate interatomic distances in the square ice. Secondary peaks (after the main ionization threshold that happens in our case at about 540 eV; Fig. 1b) arise owing to multiple scattering, and the energy separation ΔE obeys the relation[42] $\Delta E \times R^2 = C$, where R is the distance between oxygen atoms and C is a constant. Using $C = 150$ (this value was empirically determined for cubic ice[43], which is the closest approximation to square ice to be found in the literature) and an energy of about 559 eV for the prominent secondary peak in the observed EELS, we estimate $R = 2.80 \pm 0.07$ Å. The good agreement between this value and a obtained from atomic-resolution TEM images provides an independent confirmation of the crystal structure of square ice.

In principle, the interlayer separation in layered crystals can be determined by TEM imaging at different tilt angles. Unfortunately, this is impossible to achieve in practice for our nanoscale crystals, which constantly move and rotate under the electron beam. Indeed, for acquiring interpretable high-resolution images, crystals need to be oriented precisely along a zone axis and remain stationary during imaging. The reason that high-resolution imaging is possible in our case is that the graphene layers fix the orientation of ice crystals relative to the electron beam. Even though the crystals change their in-plane orientation (rotate), the [001] direction remains parallel to the optical axis of the microscope.

Analysis of TEM images. To determine the number of layers in 2D ice crystallites, we quantified the contrast from oxygen atoms using a variance filter, as illustrated step by step in Extended Data Fig. 4 and explained in its legend. This resulted in contrast maps such as that in Extended Data Fig. 4d. They show that the average contrast changes in steps of equal height. There are three distinct parts in the ice crystallite in Extended Data Fig. 4a, of one, two and three monolayers of water each.

The simulated images presented in Fig. 2b and c were obtained as follows. First, we constructed a square lattice of water molecules arranged in one, two or three layers with different stacking orders. After that, TEM images for different arrangements were simulated using QSTEM software[44] and the parameters corresponding to our experimental conditions (accelerating voltage and spherical aberration coefficient).

MD setup. Most of our simulations were done for the geometry shown in Extended Data Fig. 5. This involved two water reservoirs that contained 2,000 molecules each and were connected by a relatively long capillary formed by two parallel graphene sheets. The length and width of the graphene channel were kept at 68 Å and 56 Å, respectively. The height h was chosen to be 6.5 Å, 9.0 Å and 11.5 Å in order to accommodate one, two and three layers of water molecules, respectively. The graphene sheets were either kept rigid or allowed to be flexible during simulations. Unless stated otherwise, water was modelled using the extended simple point charge (SPC/E) model, which is described by the sum of a long-range Coulomb potential and a short-range Lennard–Jones potential[45]. The parameters for water–graphene interaction were chosen as in ref. 46. The long-range interactions were computed using the particle–particle particle–mesh (PPPM) algorithm, with a convergence parameter of 10^{-4}. Periodic boundary conditions were applied in all three directions of the simulation box.

For monolayer ice, we have also performed MD simulations for freely moving graphene sheets that 'self-consistently' enclose trapped water molecules (Extended Data Fig. 8d). For bilayer and trilayer ice, the graphene confinement observed experimentally is terraced with atomically sharp steps between ice terraces (see Fig. 2). It has proved difficult to reproduce such a terraced confinement in MD analysis. Therefore, the high pressure induced by encapsulating graphene sheets (see below) was modelled to a first approximation by applying a hydrostatic pressure P in the direction parallel to the graphene layers, as shown in Extended Data Fig. 5.

MD simulations were performed in an isothermal, isobaric ensemble, in which temperature (298 K) and pressure were controlled by the Nose–Hoover thermostat and barostat, respectively. In the equilibrium run, pressure P was kept at 1 atm (10^{-4} GPa) for 5 ns, during which time water molecules filled the graphene nanocapillary. After that, P was increased up to 10 GPa over 15 ns. A time step of 1.0 fs was used for the velocity-Verlet integrator. All the simulations were carried out using LAMMPS[47]. To determine the lattice parameter a, we counted the number of water molecules over the entire area of the graphene capillary.

Van der Waals pressure. Attractive van der Waals forces between two graphene sheets favour the adhesion of the sheets over a maximal area. If a material (for example, a gas bubble) is trapped between the sheets, the bubble will continue to shrink in size until a built-up hydrostatic pressure is able to balance the adhesion forces. For a quasi-2D confinement such as that shown in Extended Data Fig. 8a, it is straightforward to estimate the resulting van der Waals pressure, P_W. Indeed, a displacement δ of the enclosure boundary results in a gain in adhesion energy equal to $\delta \times L \times E_W$, where L is the enclosure circumference and E_W is the difference between graphene–graphene and graphene–water adhesion energies per unit area. E_W can be estimated as a typical value of the adhesion energy for van der Waals materials[29,30] because the water–graphene interaction is hydrophobic and relatively small. The above displacement requires a work of $F \times \delta$ against the internal pressure P_W, where $F = P_W \times d \times L$. For a monolayer of ice, we can use $d \approx 3.5$ Å, a typical interlayer distance in van der Waals materials. The equilibrium requires $P_W = E_W/d$, which yields ~1 GPa for $E_W \approx 30$ meV $Å^{-2}$, found experimentally for monolayer graphene[30].

To support this estimate, we have 'measured' the van der Waals pressure in MD simulations. To this end, a small amount of helium gas (1,000 atoms) was confined between freely moving graphene sheets and the system was allowed to reach equilibrium (Extended Data Fig. 8b, c). The hydrostatic pressure was estimated by

calculating the virial stress for each He atom and averaging over all of them. This has yielded a pressure of about 1.0 GPa, in agreement with the above estimate. This analysis suggests that high internal pressures are intrinsic for flexible nanoscale confinement and should generally be taken into account in studying the corresponding capillary phenomena.

MD analysis of monolayer ice. For the narrowest (6.5 Å) graphene channel, a monolayer of water was found to form an ordered square lattice with $a = 2.80 \pm 0.01$ Å for the rigid graphene confinement and 2.81 ± 0.01 Å for the flexible one (Extended Data Fig. 6), which agree well with the experimentally found $a = 2.83 \pm 0.03$ Å. Within our MD accuracy, a was found to be almost independent of pressure for all experimentally relevant P from 0 GPa to 2 GPa. At higher pressures ($P > 3$ GPa), a puckered square ice started forming.

Simulations for the realistic confinement with freely moving graphene sheets yield the same square ice with the same a (Extended Data Fig. 8d). To check that the SPC/E model provides sufficient accuracy, we also used the TIP4P/2005 model[48] of water and again obtained square ice with the same a. Extended Data Fig. 8d–f shows small ice crystals that appear in simulations using the above two models with freely moving graphene sheets, which proves the robustness of our MD results with respect to different models, at least for the case of monolayer ice.

Simulated few-layer ice. For the wider graphene capillaries (9 Å and 11.5 Å) that accommodated two and three layers of water, respectively, no lattice formation was found at pressures below 1 GPa. A typical snapshot of the water molecule configuration in a bilayer at 0.5 GPa is shown in Extended Data Fig. 7a, b. In this case, water within each layer forms an amorphous structure, not dissimilar to bulk water or amorphous ice. Locally, water preserves the standard tetrahedral coordination with hydrogen bonds connecting molecules both within and between the layers. As P increases above about 1 GPa, the simulations revealed an order–disorder transition accompanied by a sharp transformation in hydrogen bonding. One can see in Extended Data Fig. 7b, d that hydrogen bonds switch to the in-plane configuration, effectively decoupling the two monolayers of water. At the same time, within each layer water molecules form identical square lattices with the same lattice parameter as for the monolayer ice, $a = 2.81 \pm 0.01$ Å (Extended Data Fig. 7e). A similar transition was found for the trilayer water ($h = 11.5$ Å) but at somewhat higher pressures of $P \approx 1.3$ GPa (Extended Data Fig. 9). The values of P at which the order–disorder transition occurs qualitatively agree with the estimated internal pressure induced by adhesion between graphene sheets.

The order–disorder transition was further confirmed by calculations of the per-atom potential energy for water molecules in the simulated bilayer and trilayer ice, as shown in Extended Data Fig. 9c, d. The sharp drops in the potential energy at $P \approx 1$ and 1.3 GPa for the bilayer and trilayer, respectively, indicate ordering of the hydrogen bonds, which is similar to the known signature of the freezing transition for bulk water[49].

Square ice inside non-graphene nanocapillaries. To show that square ice could be common inside hydrophobic nanochannels, other than those lined with graphene, we performed MD simulations of water confined between two generic walls. The latter were simulated using the Lennard–Jones potential in the form $E = 4\varepsilon\left[(\sigma/r)^{12} - (\sigma/r)^{6}\right]$, where r is the distance from the wall to water molecules. Parameters ε and σ describe the depth of the potential well and the distance at which the potential is zero. 1,000 water molecules were placed between such walls separated by 6.5 Å. Periodic boundary conditions were applied in the directions parallel to the walls, and the simulations were carried out using the isothermal, isobaric ensemble as described above. To model capillaries with different hydrophobicity, ε was varied from 0.01 kcal mol^{-1} to 0.2 kcal mol^{-1}. This covers a wide range of surfaces from super-hydrophobic to weakly hydrophilic. Extended Data Figure 10a–d illustrates contact angles for such surfaces. Square ice was found to form at room temperature inside all the modelled nanochannels, independently of their hydrophobicity, and its lattice parameter was the same within ±1% as for graphene nanocapillaries (Extended Data Fig. 10e–h). Furthermore, we checked that a crystallographic structure of hydrophobic walls was not important for the occurrence of square ice. To this end, a monolayer of water was confined between artificial carbon walls with lattices other than the hexagonal one of graphene (for example, a square lattice). Again, we observed the same square ice with the same a. This allows us to conclude that the square ice is likely to be common inside hydrophobic channels that can accommodate only a few monolayers of water.

Further work is necessary to understand how different modelling parameters and geometries may influence the outcome of MD simulations and, for example, to explain the AA stacking for bilayer and trilayer square ice and the consequences of the terraced graphene confinement observed experimentally.

31. Longchamp, J.-N., Escher, C. & Fink, H.-W. Ultraclean freestanding graphene by platinum-metal catalysis. *J. Vac. Sci. Technol. B* **31,** 020605 (2013).
32. Meyer, J. C. *et al.* Direct imaging of lattice atoms and topological defects in graphene membranes. *Nano Lett.* **8,** 3582–3586 (2008).
33. Meyer, J. C. *et al.* Accurate measurement of electron beam induced displacement cross sections for single-layer graphene. *Phys. Rev. Lett.* **108,** 196102 (2012).
34. Egerton, R. F., Li, P. & Malac, M. Radiation damage in the TEM and SEM. *Micron* **35,** 399–409 (2004).
35. Mølhave, K. *et al.* Electron irradiation-induced destruction of carbon nanotubes in electron microscopes. *Ultramicroscopy* **108,** 52–57 (2007).
36. Yuzvinsky, T. D., Fennimore, A. M., Mickelson, W., Esquivias, C. & Zettl, A. Precision cutting of nanotubes with a low-energy electron beam. *Appl. Phys. Lett.* **86,** 053109 (2005).
37. Adrian, M., Dubochet, J., Lepault, J. & McDowall, A. W. Cryo-electron microscopy of viruses. *Nature* **308,** 32–36 (1984).
38. Zan, R. *et al.* Control of radiation damage in MoS_2 by graphene encapsulation. *ACS Nano* **7,** 10167–10174 (2013).
39. Myneni, S. *et al.* Spectroscopic probing of local hydrogen-bonding structures in liquid water. *J. Phys. Condens. Matter* **14,** L213–L219 (2002).
40. Näslund, L. A. *et al.* X-ray absorption spectroscopy study of the hydrogen bond network in the bulk water of aqueous solutions. *J. Phys. Chem. A* **109,** 5995–6002 (2005).
41. Algara-Siller, G., Lehtinen, O., Turchanin, A. & Kaiser, U. Dry-cleaning of graphene. *Appl. Phys. Lett.* **104,** 153115 (2014).
42. Natoli, C. R. in *EXAFS and Near Edge Structure (*eds Koningsberger, D. C. & Prins, R.) Vol. 3, 573 (Wiley, 1988).
43. Tse, J. S., Tan, K. H. & Chen, J. M. Oxygen K-edge XANES of crystalline and amorphous ice. *Chem. Phys. Lett.* **174,** 603–608 (1990).
44. Koch, C. Determination of core structure periodicity and point defect density along dislocations. PhD thesis, Arizona State Univ. (2002); http://elim.physik.uni-ulm.de/wp-content/uploads/talks/Koch02_dissertation.pdf or http://adsabs.harvard.edu/abs/2002PhDT.....50K.
45. Berendsen, H. J. C., Grigera, J. R. & Straatsma, T. P. The missing term in effective pair potentials. *J. Phys. Chem.* **91,** 6269–6271 (1987).
46. Werder, T., Walther, J. H., Jaffe, R. L., Halicioglu, T. & Koumoutsakos, P. On the water-carbon interaction for use in molecular dynamics simulations of graphite and carbon nanotubes. *J. Phys. Chem. B* **107,** 1345–1352 (2003).
47. Plimpton, S. J. Fast parallel algorithms for short-range molecular dynamics. *J. Comput. Phys.* **117,** 1–19 (1995).
48. Abascal, J. L. F. & Vega, C. A general purpose model for the condensed phases of water: TIP4P/2005. *J. Chem. Phys.* **123,** 234505 (2005).
49. Matsumoto, M., Saito, S. & Ohmine, I. Molecular dynamics simulation of the ice nucleation and growth process leading to water freezing. *Nature* **416,** 409–413 (2002).

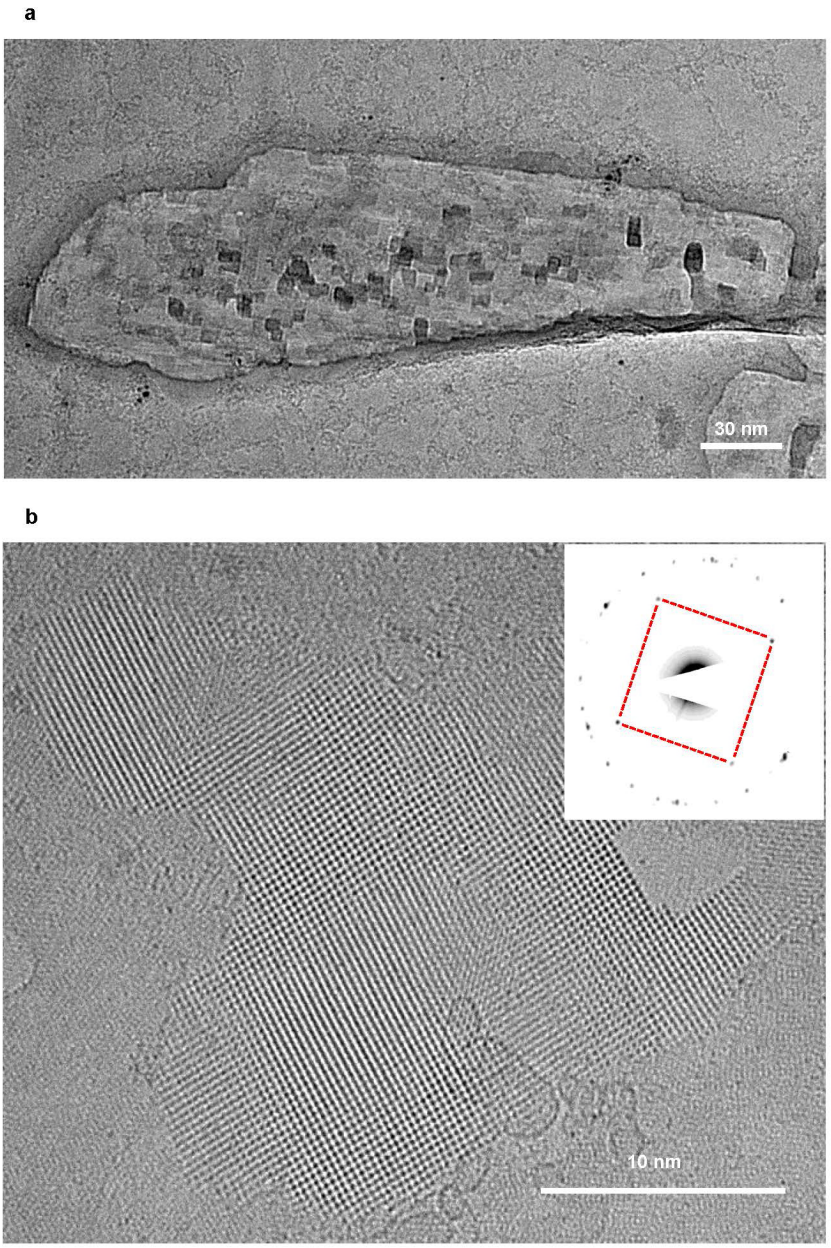

Extended Data Figure 1 | 2D water captured between graphene monolayers. **a**, Confined water at low magnification. The lateral size of such water pockets was typically ~100 nm. The chequered pattern reveals a collection of ice crystallites. **b**, Another example of a high-magnification image of 2D ice. The inset shows selected area electron diffraction from a region approximately 120 nm in diameter. The four diffraction spots connected for clarity by the red lines yield $a = 2.83 \pm 0.03$ Å, the same as the value obtained using the fast Fourier transform in Fig. 1.

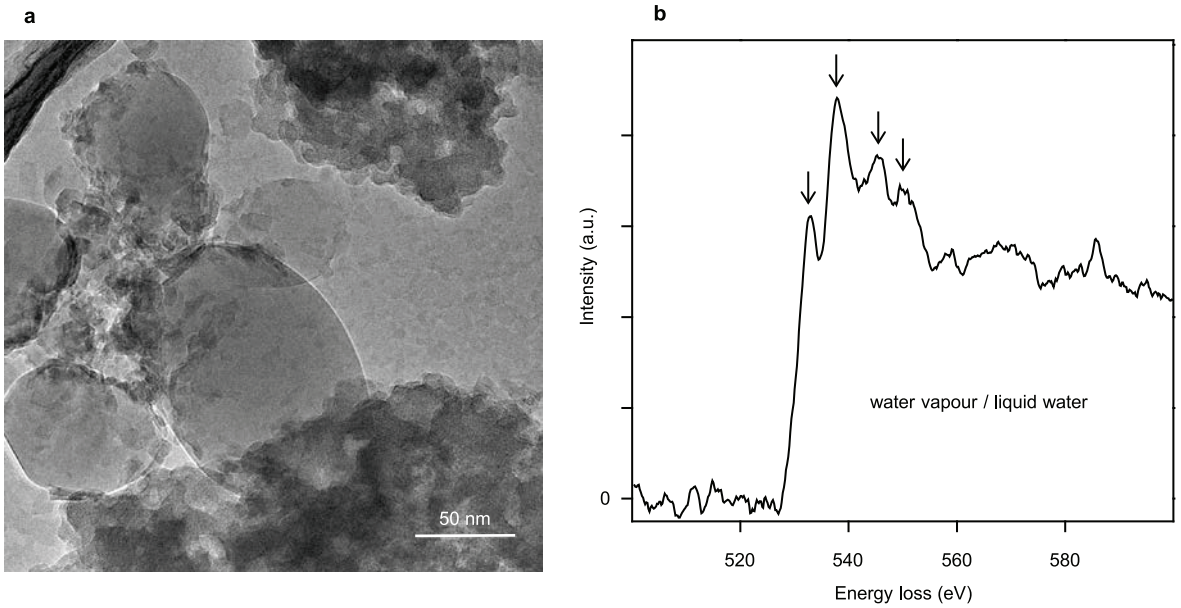

Extended Data Figure 2 | Large water droplets and their EELS. **a**, Low-magnification TEM image of a reference sample in which water was trapped in large bubbles (diameter of ~100 nm). **b**, Spectrum near the oxygen K-edge from the droplets shown in **a**. The four marked peaks at 532 eV, 537 eV, 545 eV and 550 eV are in agreement with the previously studied spectra for mixtures of water vapour and liquid water[39,40].

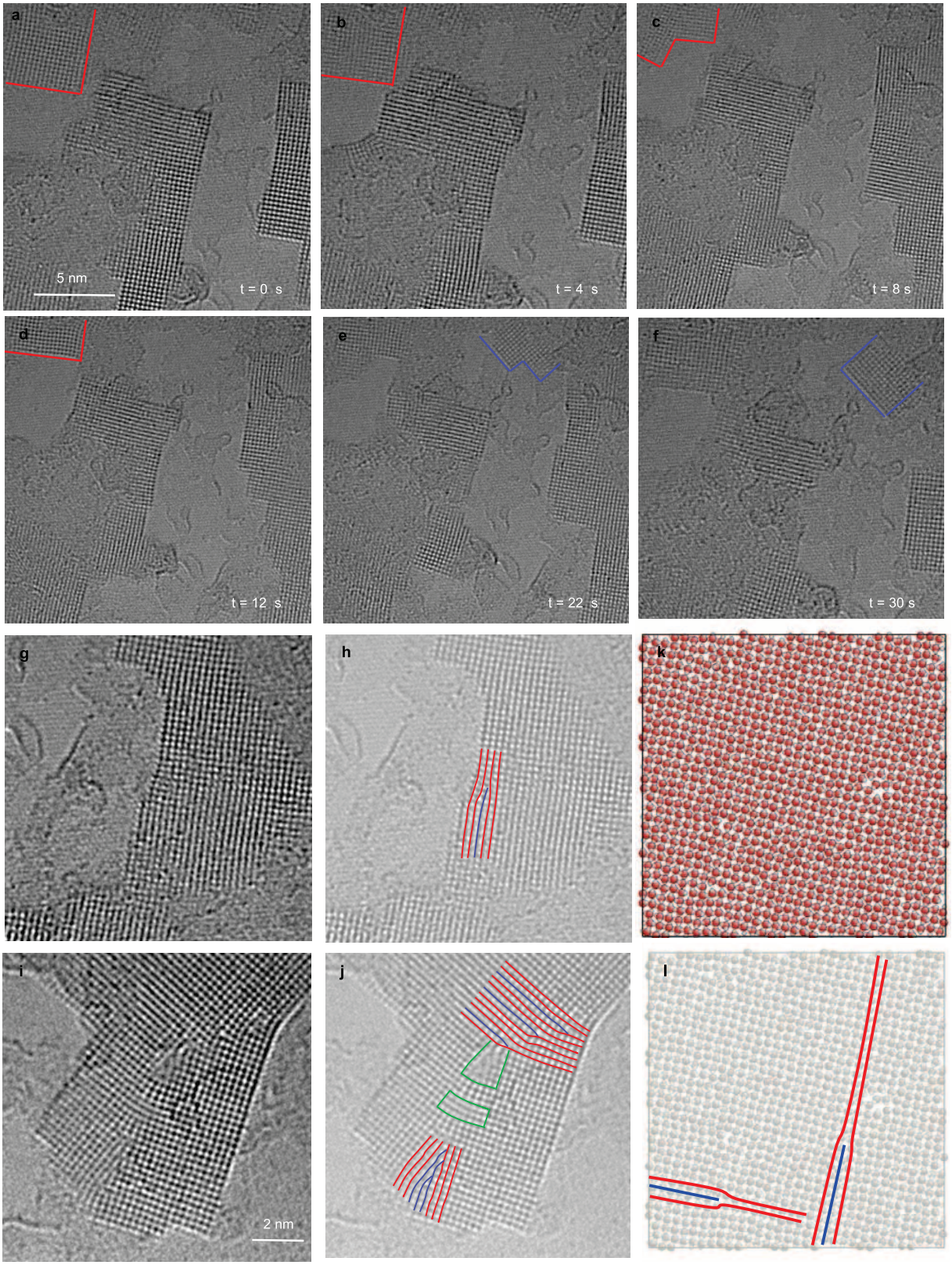

Extended Data Figure 3 | Dynamics of 2D ice crystallites and formation of defects. **a**–**f**, High-resolution snapshots from the Supplementary Video illustrate continuous reorganization of ice crystallites. Red lines highlight some of the changes: the bilayer crystal in **a** thins down to a monolayer in **b**, then splits into two crystals separated by a grain boundary in **c**, and a trilayer is formed in the same area in **d**. In **e**, a new crystallite, outlined in blue, appears in the top right corner, growing and propagating towards the centre in **f**. Other crystallites also change from panel to panel. **g**–**j**, Examples of an edge dislocation (**g**) and tilt grain boundaries (**i**) in 2D ice. **h** and **j** are the same images as **g** and **i**, respectively, but with reduced contrast; atomic rows are overlaid with red and blue lines to highlight the defects. Red lines mark existing atomic rows; blue lines mark extra rows originating from dislocations; green shapes outline defects without discernible atomic structures. **k**, **l**, Monolayer ice found in MD simulations also shows dislocations, indicating that they are intrinsic to the formation of 2D ice at room temperature.

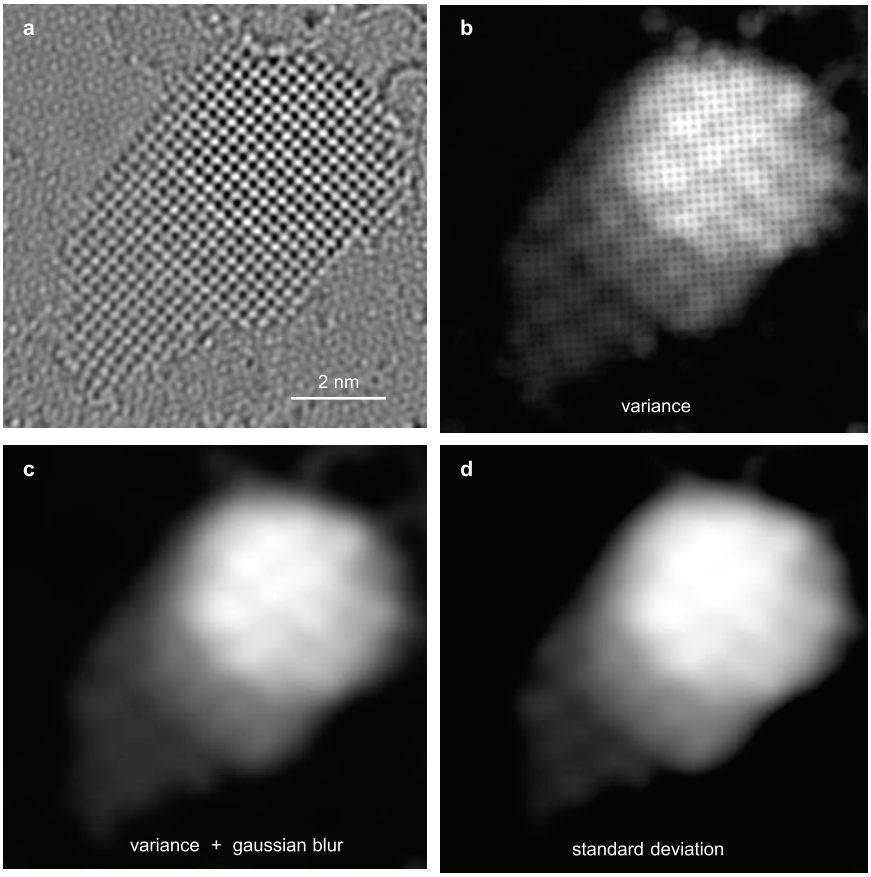

Extended Data Figure 4 | Quantifying the contrast to determine the number of layers in 2D ice. **a**, An example of the original TEM images used in our analysis (same image as in Fig. 2a). **b**, The filter calculates the local variance that is displayed as a greyscale value. **c**, The lattice pattern that remains visible in the variance image (**b**) is suppressed by applying the Gaussian blur. **d**, The final root-mean-square contrast map (that is, the standard deviation map) is obtained by calculating the square root of each pixel value of the variance image (**c**).

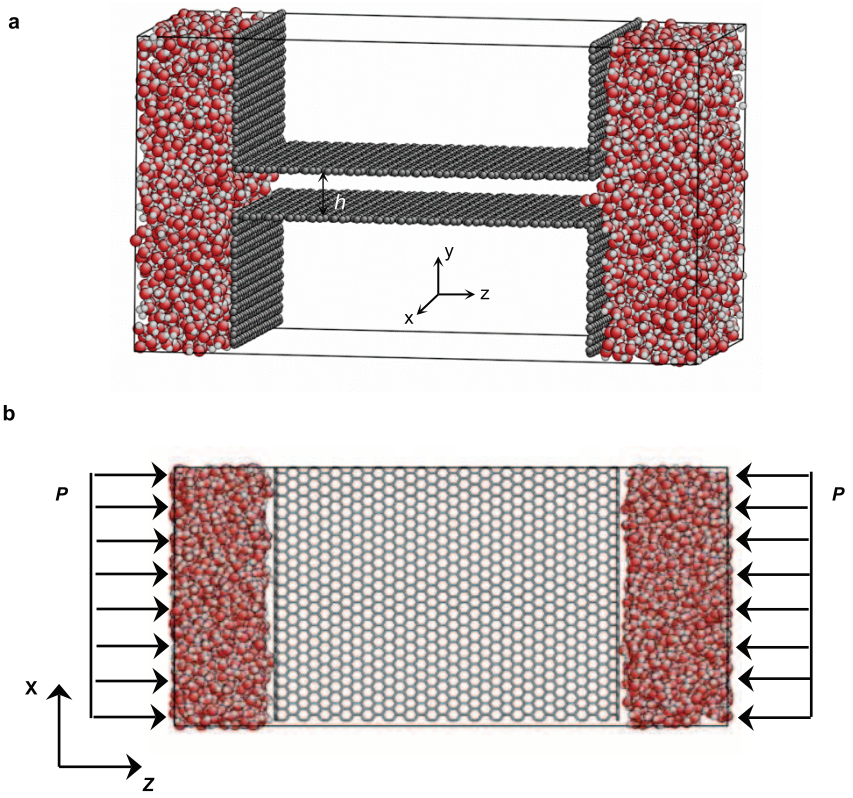

Extended Data Figure 5 | MD simulations setup. **a**, Initial configuration. **b**, Top view of the empty graphene channel, also showing how the external pressure P is applied to mimic the van der Waals pressure.

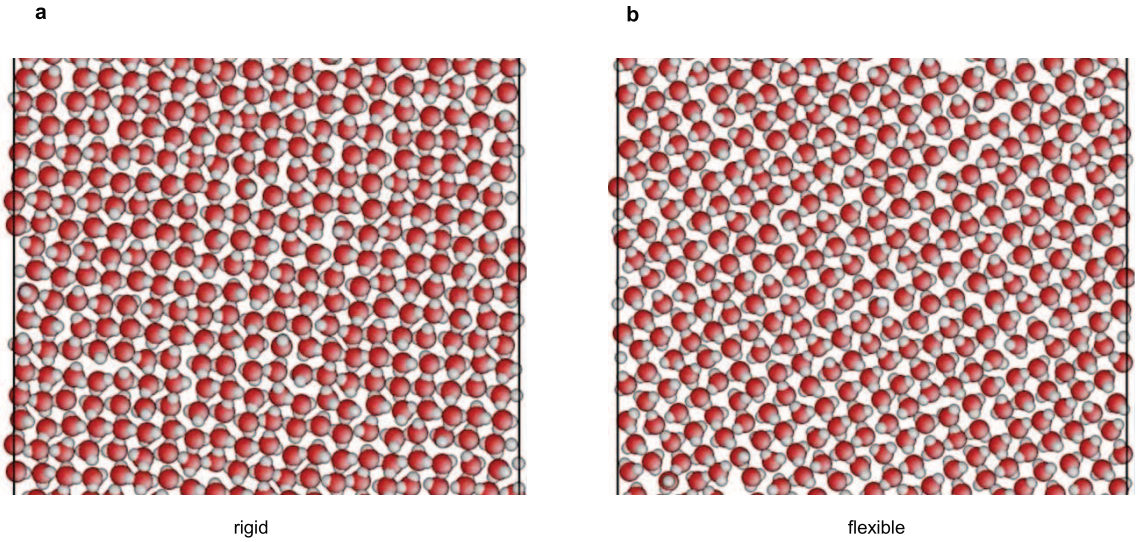

Extended Data Figure 6 | MD simulations of a monolayer of water in a 6.5-Å-high graphene capillary. Only one layer of water molecules can fit in. Red and grey circles represent oxygen and hydrogen atoms, respectively. Square ice is formed in this case, independently of whether the confinement is provided by rigid (**a**) or flexible (**b**) graphene sheets.

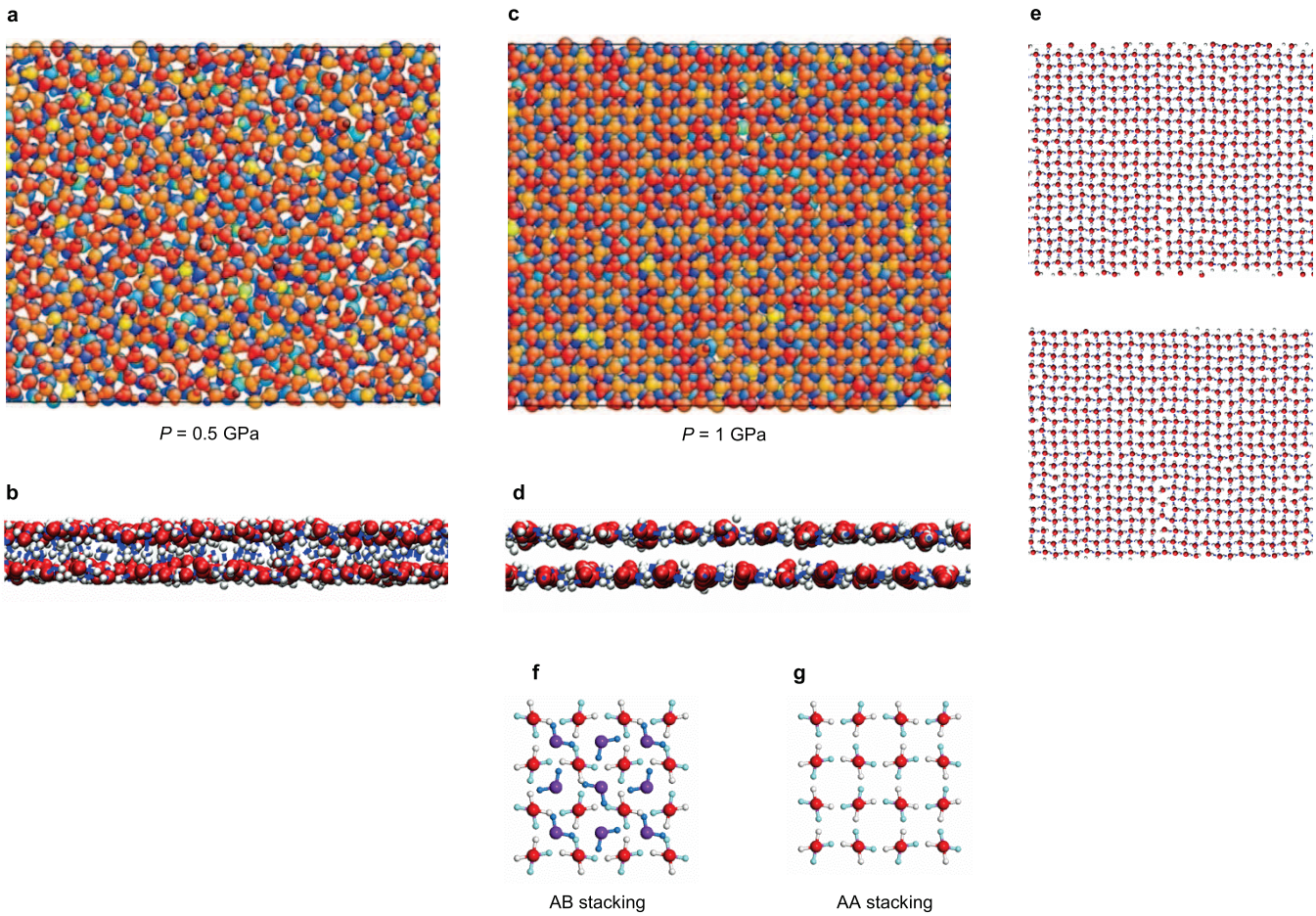

Extended Data Figure 7 | MD simulations for a 9-Å-high graphene capillary. **a, b,** Top (**a**) and side (**b**) views of a bilayer of water formed at $P = 0.5$ GPa. Different colours in **a** correspond to different vertical positions of water molecules in different layers: dark blue and red mark the bottom and top positions, respectively and lighter colours correspond to intermediate positions. Although the water molecules are clearly arranged in two layers, no intralayer ordering is present and hydrogen bonds preserve their tetrahedral coordination as in bulk water. **c**, **d**, As in **a** and **b** but at 1.0 GPa. Ordered bilayer ice is formed, with identical square lattices in the two layers, as illustrated by snapshots of the top and bottom layers in **e**. The ordering is accompanied by switching hydrogen bonds to in-plane coordination. **f**, **g**, Schematic illustration of AB and AA stacking. The stacking found in **c** and **d** is AB.

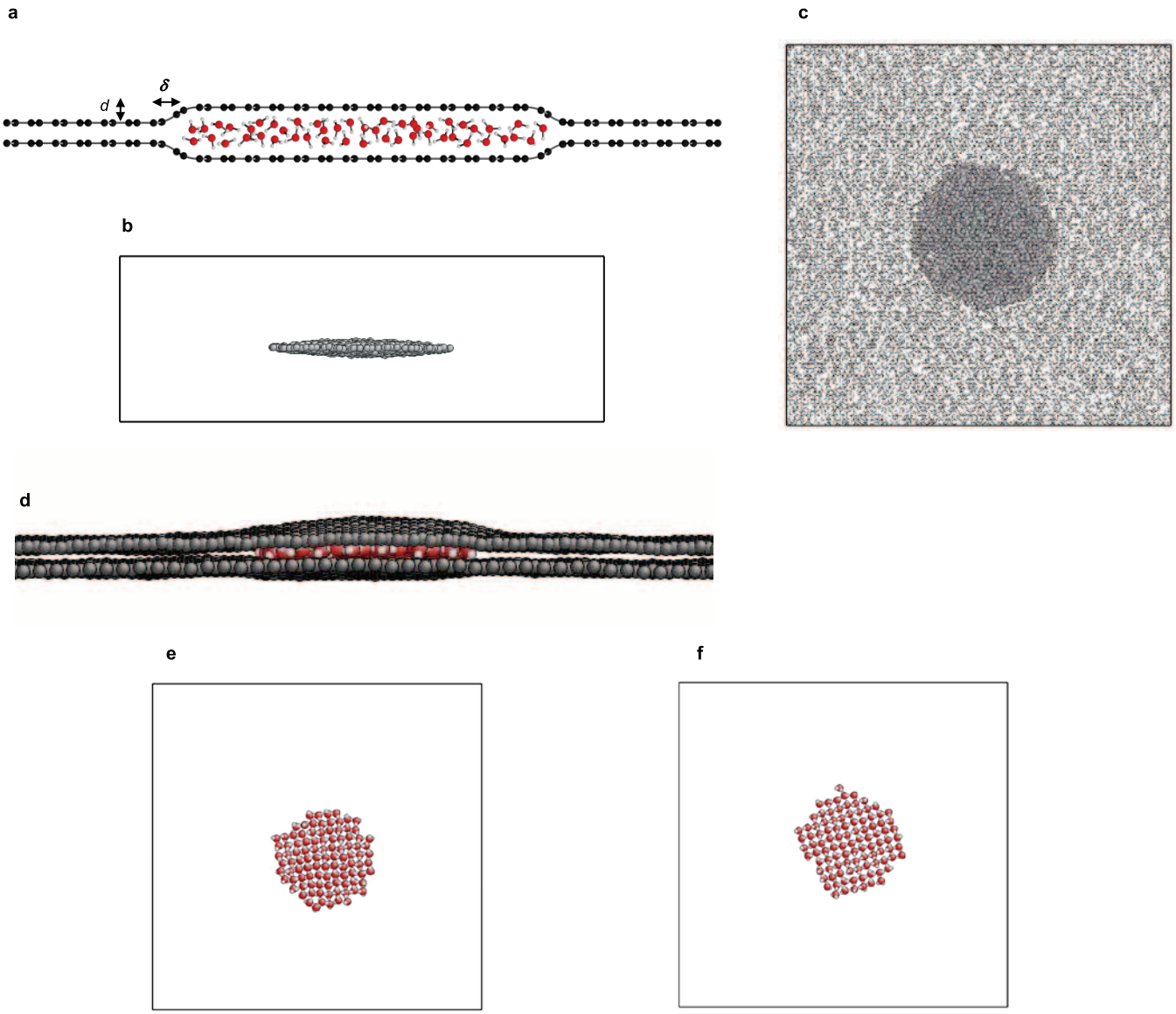

Extended Data Figure 8 | Van der Waals pressure acting on water trapped between graphene sheets. **a**, Schematic illustration of water confined by graphene. Owing to adhesion between the graphene layers, water is squeezed into a 2D puddle. Parameters d and δ are used in our estimation of van der Waals pressure (see Methods). **b**, **c**, MD simulations of van der Waals pressure exerted on a gas bubble (1,000 He atoms) trapped between two freely moving graphene sheets, showing side (**b**) and top (**c**) views of the He nanoballoon. In **b**, the graphene layers are not shown for clarity, and in **c** they are in light grey. **d**–**f**, Simulations of 2D ice formed by a water nanodroplet (100 molecules) confined between two freely moving flexible graphene sheets. Oxygen atoms are shown in red, hydrogen in light grey and graphene in dark grey: side (**d**) and top (**e**, **f**) view at equilibrium Simulations in **d** and **e** were performed using the SPC/E model and, in **f**, using TIP4P/2005. For clarity, graphene is not shown in **e** and **f**. The lattice parameter in **e** and **f** is about 2.8 Å within the modelling accuracy.

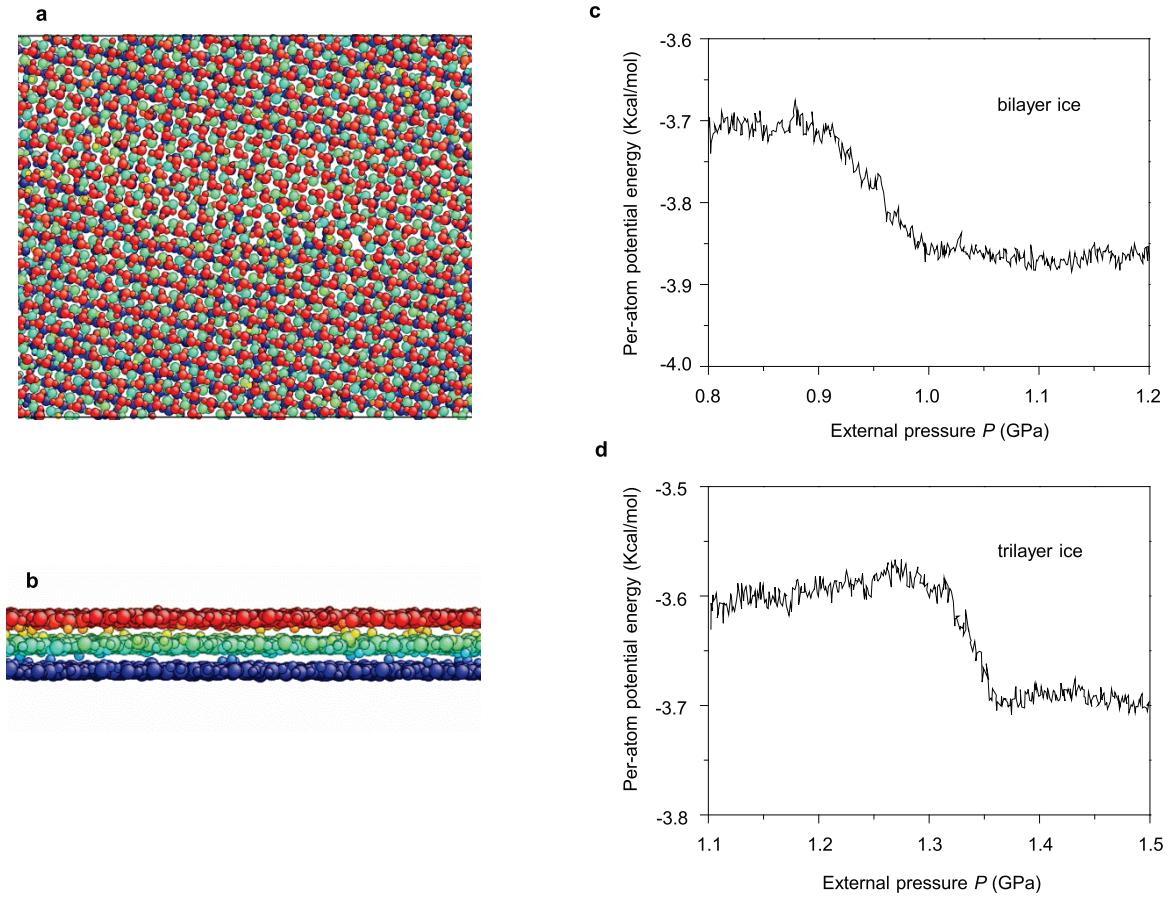

Extended Data Figure 9 | MD simulations of the order–disorder transition in trilayer ice. Top (**a**) and side (**b**) views of trilayer ice formed at $P \approx 1.4$ GPa in the graphene capillary with $h = 11.5$ Å. Different colours correspond to water molecules in different layers (same colour coding as in Extended Data Fig. 7). No clear stacking sequence can be determined for this structure. **c**, **d**, Potential energy per atom in 2D ice as a function of applied pressure for the bilayer (**c**) and trilayer (**d**) ice.

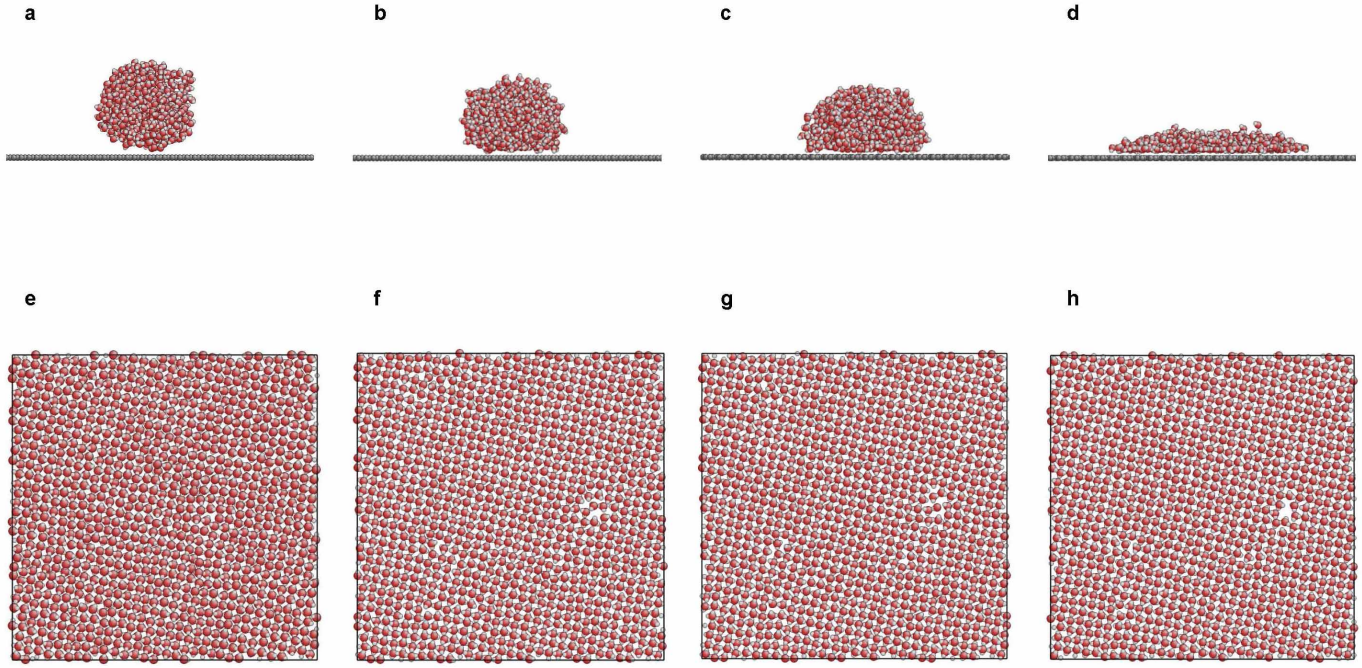

Extended Data Figure 10 | Square ice in nanocapillaries with different hydrophobicity. **a**–**d**, Water droplets on surfaces with $\varepsilon = 0.01$ kcal mol^{-1}, 0.05 kcal mol^{-1}, 0.1 kcal mol^{-1} and 0.2 kcal mol^{-1}, respectively. The changes in the relative strength of water–water and water–surface interactions result in different contact angles. For comparison, ε for the graphene–water interaction is 0.07 kcal mol^{-1}. **e**–**h**, Monolayer ice confined between surfaces with ε corresponding to **a**–**d**, respectively. In this case, the modelled walls are generic and do not have a discrete atomic structure, that is, their potential is uniform. $h = 6.5$ Å, the same as for the modelling of monolayer ice in the graphene nanocapillary in Extended Data Fig. 6.